Original research article

Computational modelling of nephron progenitor cell movement and aggregation during kidney organogenesis

Pauli Tikka [a],*, Moritz Mercker [c], Ilya Skovorodkin [b], Ulla Saarela [b], Seppo Vainio [b], Veli-Pekka Ronkainen [b], James P. Sluka [d], James A. Glazier [d], Anna Marciniak-Czochra [c], Franz Schaefer [a]

[a] *Division of Pediatric Nephrology. Heidelberg University Center for Pediatrics and Adolescent Medicine, Heidelberg, Germany*
[b] *Faculty of Biochemistry and Molecular Medicine, Biocenter Oulu, University of Oulu, Oulu, Finland*
[c] *Institute of Applied Mathematics (IAM) and Interdisciplinary Center of Scientific Computing (IWR), Mathematikon, Heidelberg University, Germany*
[d] *Department of Intelligent Systems Engineering and Biocomplexity Institute, Indiana University, Bloomington, Indiana, USA*

ARTICLE INFO

ABSTRACT

During early kidney organogenesis, nephron progenitor (NP) cells move from the tip to the corner region of the ureteric bud (UB) branches in order to form the pretubular aggregate, the early structure giving rise to nephron formation. NP cells derive from metanephric mesenchymal cells and physically interact with them during the movement. Chemotaxis and cell–cell adhesion differences are believed to drive the cell patterning during this critical period of organogenesis. However, the effect of these forces to the cell patterns and their respective movements are known in limited details. We applied a Cellular Potts Model to explore how these forces and organizations contribute to directed cell movement and aggregation. Model parameters were estimated based on fitting to experimental data obtained in *ex vivo* kidney explant and dissociation–reaggregation organoid culture studies. Our simulations indicated that optimal enrichment and aggregation of NP cells in the UB corner niche requires chemoattractant secretion from both the UB epithelial cells and the NP cells themselves, as well as differences in cell–cell adhesion energies. Furthermore, NP cells were observed, both experimentally and by modelling, to move at higher speed in the UB corner as compared to the tip region where they originated. The existence of different cell speed domains along the UB was confirmed using self-organizing map analysis. In summary, we saw faster NP cell movements near aggregation. The applicability of Cellular Potts Model approach to simulate cell movement and patterning was found to be good during for this early nephrogenesis process. Further refinement of the model should allow us to recapitulate the effects of developmental changes of cell phenotypes and molecular crosstalk during further organ development.

1. Introduction

The mammalian kidney is the product of a highly complex, orchestrated developmental process, which involves not only proliferation and differentiation processes but also directed movement and aggregation of progenitor cells [1]. Early nephrogenesis is characterized by the interplay of the branching and expanding ureteric bud (UB), the epithelial precursor structure destined to become the urinary tract, and the 'cap' metanephric mesenchyme (CM) surrounding the tips of the UB branches (Fig. 1) [2–7]. A fraction of CM cells differentiates into nephron progenitor (NP) cells, which migrate towards the corner of the UB branches where they condensate to form circular pretubular aggregates (PTA) [8]. The PTA transforms into the renal vesicle, from which the final structures of the nephron, i.e. the tubules and glomeruli, are derived in a process of elongation and invagination [7,9].

Early nephrogenesis research presumed that the speed of NP cells near PTA was approximately constant [10]. This kind of ideal behaviour of cells is not discussed here, since this kind of movement was not observed nor here or previously [9]. However, recent studies have indicated that the speeds of NP cells were not constant, since they moved in a semi-stochastic and swarming-like fashion [9], which driven by adhesion differences and/or chemotaxis [9,11]. This is henceforth designated to be the normal behaviour of the cell movements. There is no target behaviour of cells. The molecular mechanisms driving NP cell induction and PTA formation have been only partially unravelled [8,9,11–13]. UB epithelial cells secrete various diffusible signalling proteins that may trigger the differentiation of MM to NP cells as well as their chemotactic movement from UB tip region towards
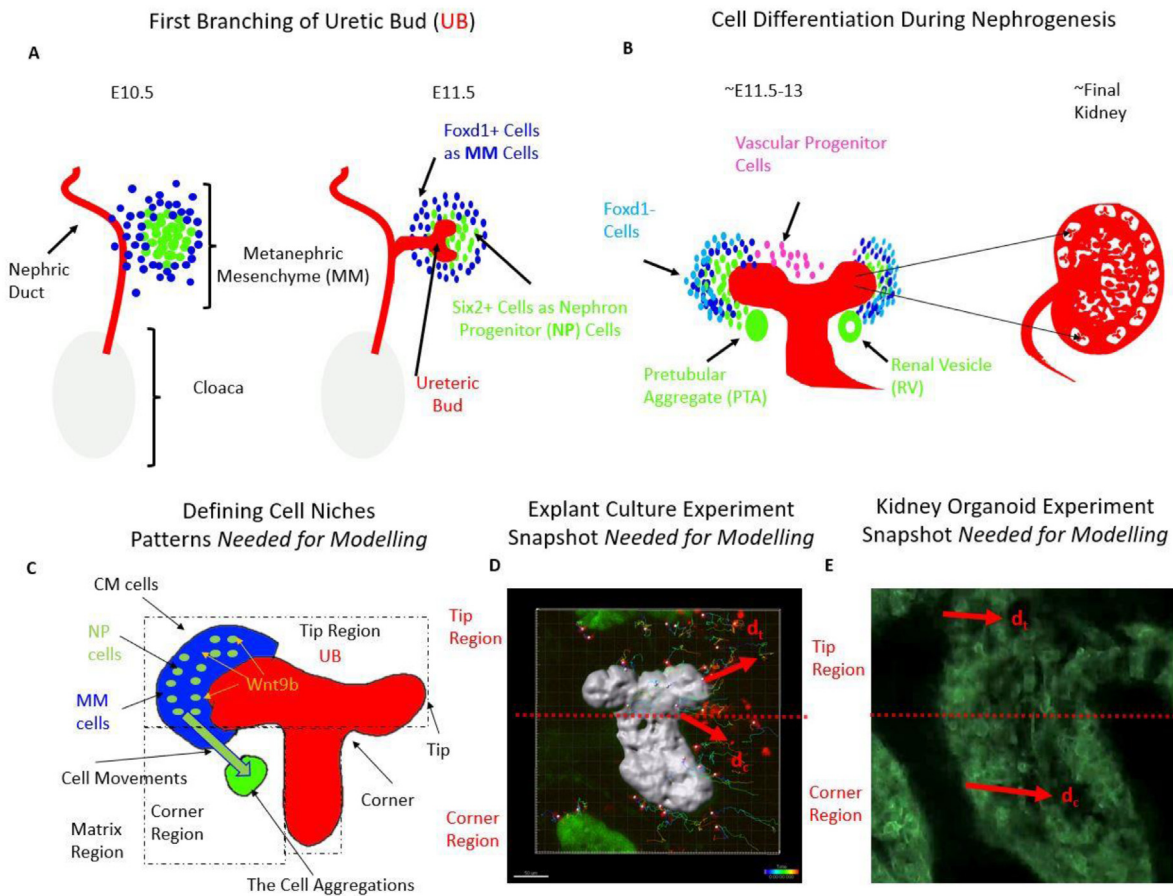
Fig. 1. Morphological structures in early nephrogenesis. (A) First branching of ureteric bud (UB) surrounded by cells of metanephric mesenchyme (MM). (B) Terminal branch of UB with cap mesenchyme (CM), pre-tubular aggregate (PTA) and renal vesicle (RV). The places of UBs are shown in relation to a schematic figure of final kidney. (C) Schematic drawing of UB trunk, corner, and tip regions with CM of NP and MM cells, with targeted movement of NP cells towards PTA according to the putatively UB derived chemoattractant such as Wnt9b that also induces some of the MM cells (with unknown order) to form as NP cells. (D) Tracks of NP cell (red) movements around UB (grey) in kidney explant culture model. Scalebar (bottom left) represents 50 μm, compare [9]. (E) Kidney organoid model with black areas representing UB, and GFP labelled MM cells. D/E) Red arrows represent vectors of tip distance (dt) and corner distance (dc) used for analysis. The figure D was by a courtesy of Dr Alexander N. Combes regarding the similar figure in [9].

the UB corner region (Fig. 1) [9,13,14]. Furthermore, cell aggregation appears to be driven by differences in cell–cell adhesion properties [15], which may also be driven by autocrine and/or paracrine intercellular signalling [16–19]. The motivation of this study was to understand more elaborately the swarmlike NP cell movements that lead to the formation of PTA in order to elucidate matters related to developmental kidney diseases.

A descriptive analysis of these processes is possible only to a limited extent, since even simple cell–cell interactions can lead to complex and unexpected large-scale patterns both in developing and final kidney [20]. Therefore, computational methods have been introduced to mechanistically analyse early nephrogenesis [9]. Combes et al. applying a convection–diffusion model, showed that attractive and repulsive cues between CM cells and the UB, together with cell adhesion processes, can lead to the commitment and maintenance of the CM in proximity to the tip (c.f., Fig. 1). However, the underlying cellular processes leading to the observed attraction and repulsion have not been analysed in detail, and the study was focused on the formation and maintenance of the CM rather than the formation of the PTA.

In this study we used a computational modelling approach to explore in detail the biophysical mechanisms underlying the directed movement and aggregation of NP cells, the critical first step of nephron development [7,8]. We extended the pioneering work of Combes et al. by systematically simulating chemical and mechanical cellular processes that potentially explain pattern formation during early nephrogenesis and used 3D tissue simulation approaches to analyse how cell chemotaxis induced by different sources of chemoattractant and

adhesion differences between different cell types may explain the formation of both the CM and the PTA. Parameter calibration and model validation was achieved by comparison of the simulation results with both published and original experimental data.

2. Methods

2.1. Model construction

We applied Cellular Potts Model (CPM) to describe the behaviour (movement and aggregation) of NP and MM cells during early murine nephrogenesis (postconceptional day 12) and used the CompuCell3D software (CC3D) for this purpose [9,14,15,21]. Mathematical details of the developed CPM are given in the supplements (Cellular Potts Model; Eqs. 1–3, and 7 in appendix). The following general assumptions were made to adjust CPM [9,14]:

1. NP, MM, and matrix cells can move caused by cell sorting (as described in CPM chapter) [9,22].
2. Matrix cells are chemically and physically neutral in comparison to other cells [9] and have low or insignificant (close to zero) value of adhesion between other cells and are not affected by nor emit any chemical gradient in CPM
3. Only NP cells are able to perform chemotaxis, while UB, NP, or both cell types can secrete a chemoattractant [23].
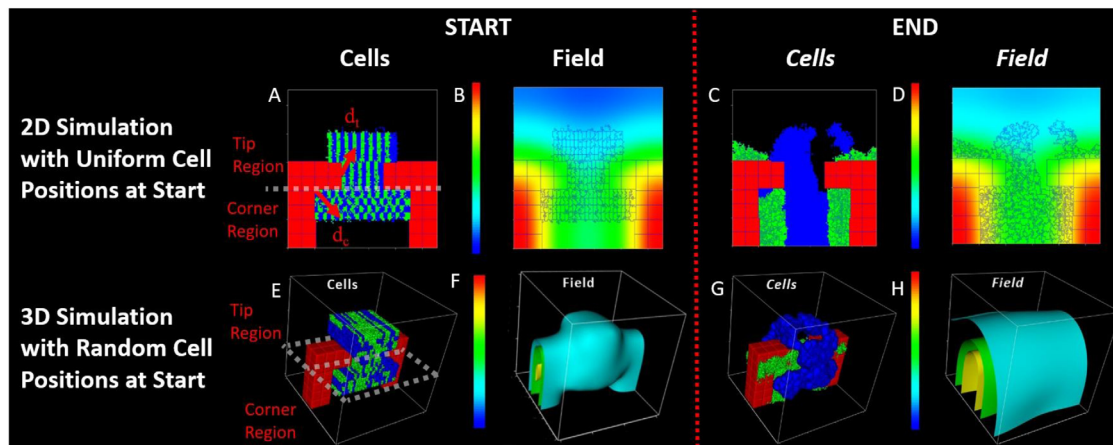4. UB cells are static ("drift corrected UBs" [9]).

Fig. 2. Two-dimensional (A–D) and three-dimensional (E–H) simulation patterns obtained with model 7_UB_NP_ADH. A/E) Initial cell patterns with uniform (A) and random (E) cell positions; tip distance (d_t; [40,50]) and corner distance (d_c;[20,40]) vectors are depicted in (A). Corner region is y ≤ 40 both in 2D and 3D simulations. B/F) Initial chemoattractant gradient patterns from UB. C/G) Final cell patterns. D/H) Final chemoattractant patterns from UB. In panels A, C, E, and G UB cells are depicted in red, NP cells in green and MM cells in blue, while matrix space appears black. In panels B, F, D, and H, standardized chemoattractant concentration gradients are depicted by coloured areas (2D) or sheets (3D), ranging from 0 (blue) to 1 (red).

5. All cell types undergo neither proliferation nor apoptosis during the period of the observation [8,24,25].

The initial (3D) CC3D model setting comprised 2 L-shaped structures composed of 64 UB cells each separated by a space filled with MM and NP cells (n = 196 each), and a matrix compartment comprising all remaining empty (pixel) space [26]. The setting mimicked the spatial structure of two adjacent UB branches with surrounding metanephric mesenchyme (Fig. 2) [9,27]. The CM cells initially surrounding the UB tips consist of MM cells, which have similar cell volumes, masses, and general regulation mechanisms (Fig. 1C). NP cells are induced from CM cells at the outset of the modelled period [22]. All cells were set to cubical shape, with initial cell surface areas of 375 μm [3] for the MM and NP cells and 1000 μm [3] for the UB cells. The distal end of the UB branch structure was denoted as "tip region" and the origin of the inner angle of UB as "corner region" (Fig. 2C). Our primary interest was to analyse the model cell outcomes in the corner region, where the PTA is formed (Fig. 2C–E).

2.2. Simulation studies

Eight model variants were constructed to simulate the impact of (a) chemotaxis of NP cells related to chemoattractant secretion from NP and/or UB cells separately or together with (b) adhesion-based cell sorting related to adhesion differences between different cell types. The model characteristics are listed in (Table 1). These variants represented the mechanisms potentially driving the cells in the studied experimental biological systems (*ex vivo* kidney and renal organoid), which corresponded the evaluated in vivo early nephrogenesis [9].

The first model variant (1_REF) included only miniscule mechanical differences between NP and MM cells just enough to obtain patterns of 'random walking'. This model served as a reference, or minimum model. The second model (2_REF_ADH) assumed differences in adhesion energies between NP and MM cells [15] but no chemotaxis processes. Models 3 and 4 introduced chemotaxis of NP cells, assuming chemoattractant secretion either by the UB cells (3_UB) or the NP cells themselves (4_NP), while adhesion properties of NP and MM cells were set equal. In models 5 and 6, models 3 and 4 were augmented by adding adhesion energy differences between NP and MM cells (5_UB_ADH, 6_NP_ADH). The seventh model included all features, i.e. chemotaxis of NP cells, adhesion differences between NP and MM cells, and chemoattractant secretion by both NP and UB cells (7_UB_NP_ADH). Finally, a multi-adhesion model (8_ADH_ADH) was tested with adhesion differences between all cells in the model (except UB–UB). For analysis and

interpretation, models 3, 5, and 7 were categorized as 'UB secreting models', 4 and 6 as 'NP secreting models', 1, 2, and 8 as 'non-secreting models' and (2, 5, 6, 7, and 8) as 'adhesion-based models'.

The following model characteristics were permutated in the models to test their effect on cell movement and aggregation in the different model variants: (i) Initial (NP and MM) cell positions; (ii) initial spread of the chemoattractant from UB or NP or both [9]; (iii) cell–cell adhesion properties, especially of the moving NP and MM cells [15]. For this purpose, we tested NP and MM cells with random (R) or uniform (U) initial cell distribution together with the spread of chemoattractant by simulations with or without the initial presence of a chemoattractant field (Fig. 2, Table 1).

Each model variant was simulated only 30 times partly due 3D simulation times, but mainly because our 3D simulations had more than 400 cells having multiple pixels with the connected parameters elaborated below [28]. During each of these basic simulations (8 × 30 × 4 = 960), we recorded both the centre of mass (COM) of the moving cell types (NP and MM) and the relative amount of chemoattractant in these COMs over 1000 Monte Carlo Steps (MCS; Cellular Potts Model). With these COM values, we calculated the average speeds, distances, and the local concentration of the chemoattractant separately in the tip and corner regions (Figs. 1C, 2A, S1, see 'Model Simulations' and 'Technical workflow'). The cell speeds in the corner and tip regions were denoted as 'corner speeds' and 'tip speeds', respectively. Similarly, the distances of these cells from the outermost point of the UB tip were denoted as "tip distances" and the distances from the UB corner as "corner distances" (Figs. 1C, 2A). For direct comparison, the ratio of the tip to the corner values of the speeds, distances, and concentrations were calculated. Exemplary 3D model simulation snapshots are shown in Fig. 2.

2.3. Computational estimation of model parameters

Two computational schemes were elaborated for estimating the parameters of the model variants in order to investigate the qualitative and quantitative differences in the respective simulations.

The process of model parameter estimation was initiated by varying values in a 2D cell-sorting simulation study using the CC3D software as described in the (back-inducing) strategy mentioned below (see also Cellular Potts Model in the appendix) [9,21,26,27,29]. The initial parameters of spatial relationships (such as λ_A, λ_V, V_t, A_t in Eq. 2 at the supplement) and the cell numbers were chosen to be in comparable ranges as observed in the explant culture and kidney organoid experiments (see experimental data sources and Figs. 1, 2).

These initial settings constituted the reference model 1. The initial parameter ranges for the contact energy coefficient (J), which refers to the cell–cell adhesion differences [11,15], and chemotaxis strengths (λ_{CL}) [8,9,11–13] were taken from the respective literature for the other 2D models (2–8) [20,26]. The parameter values for all 2D models were subsequently scaled to 3D by multiplying by two as explained in [20], given the neighbourhood order of three. The final parameter values for the 3D models are given in Table 1. The details of parameter estimation methodology including Particle Swarm Optimization (PSO) is given in the supplement.

2.4. Self-Organized Maps (SOM)

The Self-Organized Map (SOM) approach, an iterative machine learning method [30], was applied to identify and compare especially stable cell speed regions in the simulations and experiments. Specifically, we sought to compare if the simulated and real NP cells behaved differently at the tip and corner regions respectively. The Python function 'MiniSom' [31] was applied to compare the SOM results derived from our simulations with the experimental data of Combes et al. [9] Details of the implementation are given in the supplement (see Eq. 7 in the appendix).

2.5. Experimental data sources

In this study, two sources of *ex vivo* experimental data were used to calibrate and validate the simulation models [9,32]. These comprised results obtained with an explant culture model reported by Combes et al. (2016), and original results reported in this work obtained with a dissociation–reaggregation kidney organoid model [4,9,14,32]. The data consisted of the images recorded during the experiments (see Microscopy methods below). The sizes of the recorded data frames (number of samples per number of time points) were 15 x 50 (for explant culture in 12.5–15 h) and 1 × 15 (for kidney organoid study in 2.5 h; see 'Technical Workflow' for more details). The explant culture experiments of Combes et al. comprised 500 NP cells, whereas the kidney organoid studies presented here comprised of 500–2000 MM cells. Outliers were replaced with a moving average of three previous data values; see python code 'rolling mean'.

2.6. Kidney organoids

Embryonic kidneys were dissected from embryonic day 11.5 mouse embryos from crossing of Wnt4Cre [33] and tomato floxed Rosa26 Green fluorescent protein (GFP; mT/mG) reporter mice [34] as described in [23]. Intact UBs were treated with GDNF and dissociated MM with BMP7 and FGF2 as in [23]. The intact UB was reaggregated with MM cells and incubated overnight to form a kidney organoid. The organoids were set to grow in a FiZD culture [14] for time-lapse imaging into a temperature and gas controlled on-stage incubator (OkoLab, Italy) on a Zeiss LSM780 confocal microscope.

Animal care and procedures were in accordance with Finnish national legislation for the use of laboratory animals, the European Convention for the protection of vertebrate animals used for experimental and other scientific purposes (ETS 123), and the EU Directive 86/609/EEC. The mouse studies were approved by an ethics committee by the name of 'Renaltract' (http://renaltract.eu/, including Drs Franz Schaefer and Seppo Vainio), as mentioned in the original project agreement bound by the previously mentioned legislation.

2.7. Microscopy, image processing and data segmentation

In order to track and distinguish MM cells from UB cells, MM cells were expressing GFP. The fluorescence microscopy of this work was performed with a Zeiss LSM 780 confocal microscope (Carl Zeiss, Germany) using 25x/0.8 Zeiss LCI PlanNeofluar water immersion objective with a 488 nm wavelength for excitation and a range of emission from 490–601 nm. Out of original images of 250 μm × 300 μm × 29 μm (XYZ), an area of two close and relatively static UBs (approx. 150 μm × 100 μm) was selected with the Zen Blue (Carl Zeiss, Germany) imaging program. There were 16 Z-layers in the (z axis) stack from which all were selected. Here, XYZ pixel size was 0.24 μm × 0.24 μm × 1.46 μm and the temporal resolution was given by 16-time frames with 10 min between the frames. The video of the moving MM cells in the kidney organoid experiment is given stack-by-stack in [35]. Deconvolution was used to improve image signal to noise ratio, contrast and resolution. This process was done with Huygens Professional program (Scientific Volume Imaging, The Netherlands) using distilled PSF, with background value of 3.5, S/N value of 10, autobleach correction off, and saving the resulting deconvolved image as 16-bit tiff file format [14]. The segmentation of the tiff file of the deconvolved image was done with a previously compiled in-house MATLAB code [14]. The code produced a raw data file, .csv, of the positions, sizes and speeds of all of the cells by identifying objects that it redeemed as cells from the images. We specified the cell diameter range between 0.5–20 μm.

3. Results

3.1. Initial model parameter estimation

The initial parameter settings for λ_A, λ_V, V_t, A_t, and J (see Eqs. 1 and 2 in Supplement) and the predefined spatial relationships defined the reference model (model 1, Table 1, Fig. 3A). Starting from these settings, the contact energy coefficients (J) between NP, MM, UB cells and the matrix were modified, yielding the adhesion-based models 2 and 8 (Table 1). The purpose of this modification was to identify the range of contact energy coefficients required to induce cell aggregations, and to explore the aggregation behaviour of NP and MM cells in the CC3D model space (Fig. 3B/C) [9,26,27,29].

Next, the impact of chemotaxis on cell patterning was investigated, assuming secretion of chemoattractants by UB cells and/or NP cells themselves. To that end, parameters related to chemoattractant secretion (S), diffusion (D), degradation (γ), and chemotaxis strength (λ_{CL}) were introduced (see Eqs. 2, 3 in Supplement). To derive plausible value ranges for these parameters and explore the effect of chemotaxis on cell clustering, NP cells (model 4; Fig. 3D) or UB cells (model 3; Fig. 3E) were assumed as alternative sources of chemoattractant secretion. Finally, the combined effects of the contact energies and chemotaxis were considered in the remaining models (5,6,7; Fig. 3F–H).

3.2. Simulated pattern formation

The eight model variants yielded distinctly different final cell patterns (Fig. 3). The initial conditions, including random and uniform cell starting patterns (see methods), and initial parameters (Table 1) had only a limited effect to the final cell patterns (Figs S2, S3). Therefore, the following description refers to the model patterns obtained with optimized simulations using random initial cell distribution and no pre-formed chemoattractant gradient.

The reference model yielded a cell pattern without coherent clustering over time (Fig. 3 A). The models involving chemoattractant secretion by NP cells with and without cell adhesion differences resulted in cell aggregates between the UB tips without adherence to the UB surface (Fig. 3D/F). In the models assuming adhesion differences between MM and NP cells but no chemotaxis, streak- or ball-like clusters emerged throughout the inter-UB area (Fig. 3B/C). In the models
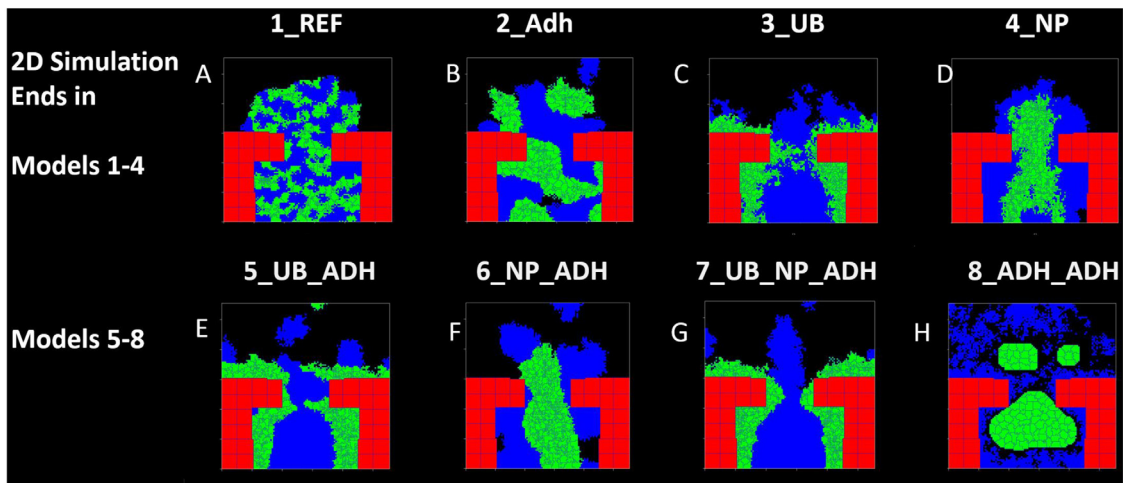
Fig. 3. Final cell configurations obtained by 2D simulation with eight different models: (A) 1st Reference (1_REF), (B) 2nd Adhesion-based (2_ADH), (C) 3rd UB secreting (3_UB), (D) 4th NP secreting (4_NP), (E) 5th UB secreting with the adhesion-based (5_UB_ADH), (F) 6th NP secreting with the adhesion-based (6_NP_ADH), (G) 7th UB and NP secreting with the adhesion-based (7_UB_NP_ADH), and (H) multi-adhesion-based (8_ADH_ADH) model. UB cells are depicted with red, NP cells with green, and MM cells with blue colours. Optimized parameters were calibrated to experimental cell properties and used in the simulations.
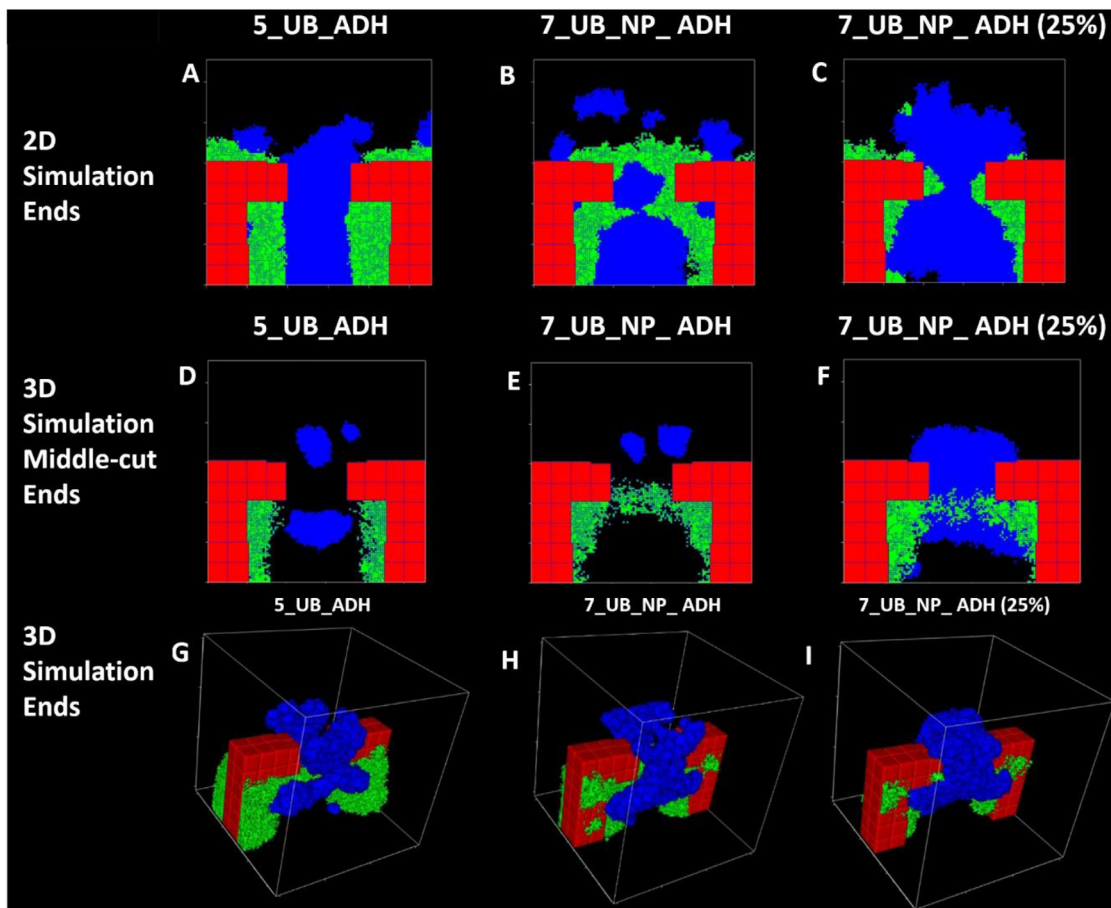

Fig. 4. Representative final cell configurations obtained with the optimized models using initial chemoattractant fields. Model simulations of 5_UB_ADH_R (A/D/G) and 7_UB_NP_ADH_R (A/D/G and B/E/H) were either in 2D (A–C) or 3D (D–I), assuming both the normal 50% or 25% (C/F/I) NP cells among total CM cell population. 3D views (G–I) are displayed together with their central transversal cuts (D–F). UB cells are depicted with red, NP cells with green, and MM cells with blue colours.

involving UB cell chemoattractant secretion, NP cells aggregated along the UB surface, with preference to the corner regions (Fig. 3E/G/H).

Directed migration and preferential aggregation of NP cells in the UB corner was observed with the models 3, 5, and 7 (Figs. 3E/G/H and 4), resembling the formation of PTA in the corner region during nephrogenesis (Fig. 4C). The most consistent formation of NP cell clusters resembling PTAs was observed with model 7, which involves chemoattractant secretion by both UB and NP cells and stronger adhesion between NP and MM cells relative to other models (Figs. 3H, 4B/E/H or C/F/I). The video of the model (7) behaviour can be viewed online [38].

Table 1
Model parameters with pre-set values applied in 3D simulations.

Parameter	Pre-set value	Models	Reference
Target volume (V_t)	375×10^{-18} m³	1–8	This work and [9]
Lambda volume (λ_V)	20×10^9 kg m⁻⁴ s⁻²	1–8	[26], [29]
Target surface area (A_t)	312×10^{-12} m²	1–8	This work and [9]
Surface lambda (λ_A)	0.1×10^{-3} kg m⁻² s⁻²	1–8	[26], [29]
Time step (MCS)	0.017 h	1–8	[26], [29]
Surface temperature (T)	20	1–8	[26], [29]
Contact energy coefficient (J)	(all cells): 5×10^{-15} kg s⁻²	1,3–4;	[26], [29]
	(NP&MM): 13×10^{-15} kg s⁻²	2, 5–7, 8ª	
Chemoattractant secretion (S)	3 DU/s	3–7	[26], [29]
Chemotaxis lambda (λ_{CL})	100×10^{-27} kg m² s⁻²	3–7	[26], [29]
Global diffusion constant (D)	1.0×10^{-12} m² s⁻¹	3–7	[26], [29], [36], [37]
Global decay constant (γ)	1.0×10^{-7} s	3–7	[26], [29]

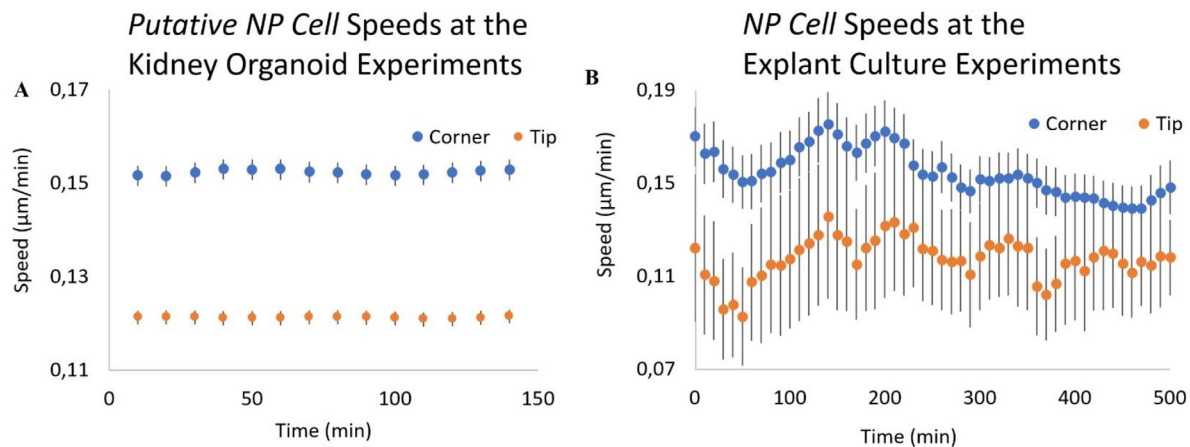ªSee Table 2 for description of multiple adhesion interfaces in model 8.

Fig. 5. Cap mesenchyme cell speeds observed in (A) kidney organoid experiments, (B) explant culture studies [9]. Cell speeds in corner region are represented in blue and cell speeds around tip in orange. Dots represent means and vertical bars 95% confidence intervals (with sample sizes of 50 and 15 for explant and kidney experiments, respectively).

3.3. Experimental studies

The results of the cell movement analysis performed on the explant culture model experiments of Combes et al. [9,15,22] and our own experiments with a dissociation–reaggregation kidney organoid model are provided in (Figs. 5–7) [30–32,39,40].

The observed overall NP cell speed averages were 0.15 ± 0.02 μm/min in the explant cultures, and $0.13 \pm 0.01 = $ μm/min in the kidney organoid MM cells.

While cell speeds in the explant culture fluctuated considerably more than in the kidney organoid experiments, in both experimental settings the two cell types moved at different rates depending on their location relative to the UB tip (Fig. 5). In the corner region, the average cell speeds were 0.16 ± 0.02 μm/min in the explant culture experiments and 0.15 ± 0.01 μm/min in the kidney organoid [9]. Average speeds in the tip region were 0.12 ± 0.01 μm/min in both experimental settings. The slower relative cell movement of both MM and NP cells around the UB tip region was also apparent when expressed as the tip-to-corner speed ratio, which was below 1 for most of the observation time (Fig. 6). According to 2D SOM analysis, stable speeds in the explant culture data were 0.19 ± 0.02 μm/min in the corner, and 0.14 ± 0.01 μm/min in the tip region [9,30]. 2D analysis was performed, because the 3D data's z coordinate values in the explant culture experiments were found to be measured partly incorrectly or by accident too high when z stack coordinate values were compared to each other. Stable cell speeds of the kidney organoid data (calculated by 3D SOM analysis) were 0.25 ± 0.02 μm/min in the corner and 0.18 ± 0.02 μm/min in the tip region respectively. The different speed of motion of cells in the tip and corner regions is illustrated in the coloured speed contours of the transformed SOM plots (Fig. 7) [30–32,39,40].

3.4. Estimation of final model parameters with particle swarm optimization and resulting cell patterns

The parameter ranges for PSO were chosen according to the initial model parameter estimates mentioned in methods also considering the applicable limits of PSO settings (detailed further in the appendix). The optimization procedure aimed at maximizing the amount of NP cells at the UB surface while simultaneously aligning the NP cell speeds in the model to the cell speeds observed experimentally in the explant culture setting, as mentioned in the methods.

The final model parameter values obtained by the PSO technique are given in Table 2. The improvement of the models achieved by the application of PSO is illustrated by the Best Quality Values (Table 2; lower numbers indicating better quality). The best model quality was obtained for model 7, while the other models showed either substantially lower quality or a spuriously high quality without matching the experimental situation. This applied in particular for the NP secreting models 4 and 6 and the adhesion model 8, where cells did not aggregate towards the UB surface in the first place.

In the optimized models, the calculated total distance travelled by the NP cells during the simulation period was between 90–160 μm. The optimization procedure resulted in a more accentuated difference in corner and tip cell speeds in the models involving chemoattractant secretion by the UB (3, 5, 7 in Fig. 6). The optimal tip-to-corner speed ratio of NP cells in these models decreased with time, aligning with the NP cell speed ratio observed towards the end of the explant culture experiments (Fig. 6B). By contrast, the MM cell speed ratios in the kidney organoid experiments were better matched by the optimized NP secreting models (4 and 6; Fig. 6D). Nevertheless, the absolute speeds in the secreting models (3–7) for the NP cells both in the tip and corner
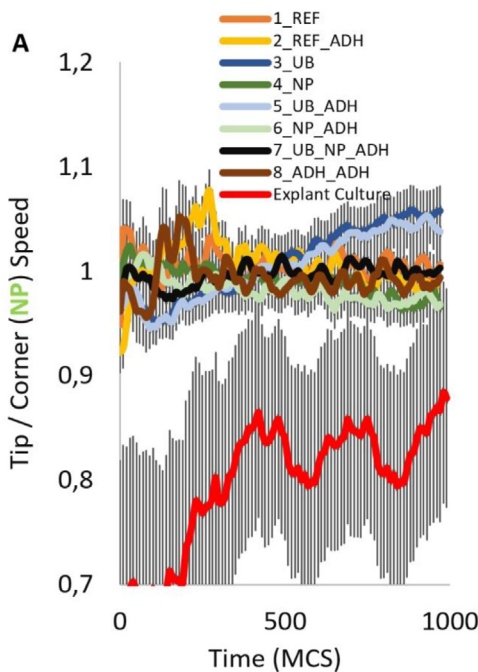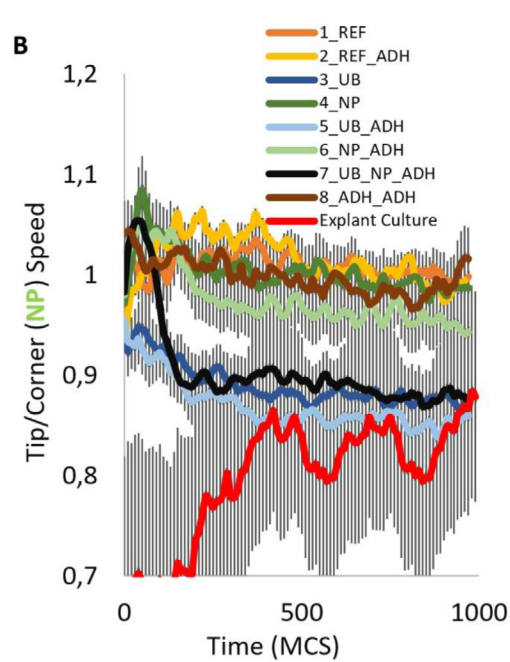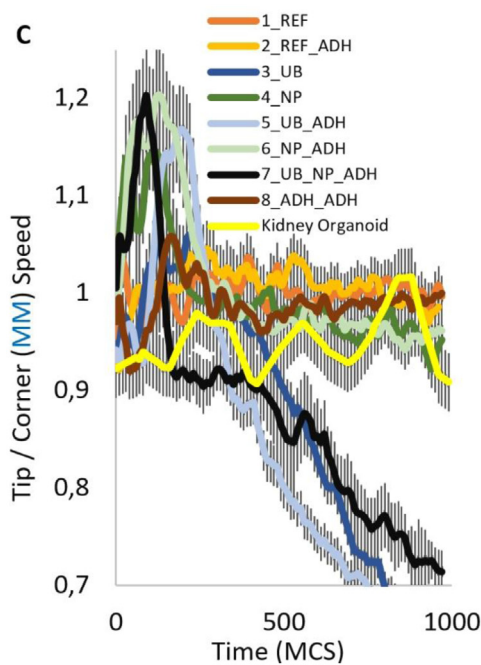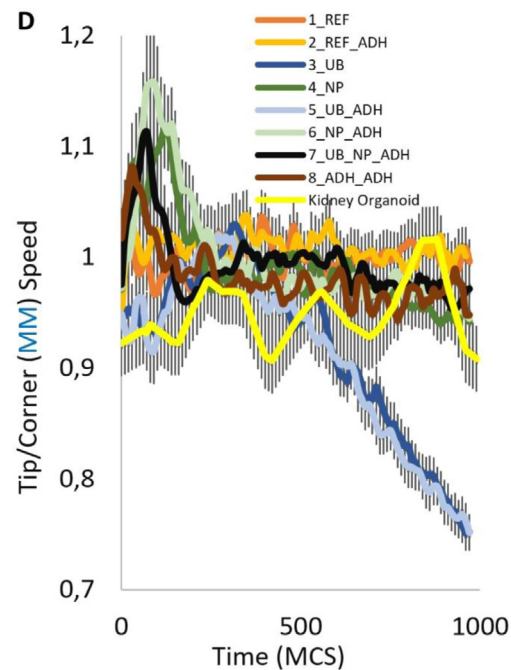
Fig. 6. Average tip-to-corner speed ratios of NP and MM cells in the simulation studies of different models together with the results from experiments. (A/B) NP cells in the models (see legend) with the cells in the explant culture experiments (scaled to model 3 and 4) [9]. (C/D) MM cells in the models similarly scaled with cells in the kidney organoid experiments. (A/C) Simulations before the optimization. (B/D) Simulations after the optimization. Vertical bars indicate 95% confidence intervals from simulations (sample size: 30) or experiments (sample sizes of 50 and 15 for explant and kidney experiments, respectively).

regions consistently exceeded those of the MM cells (0.13 ± 0.03 v. 0.03 ± 0.02 μm/min). The different speeds of cells in the tip and corner regions has been also illustrated for the experiments and model 7 by the

coloured speed contours of the transformed SOM plots (Fig. 7) [30–32, 39,40]. Correspondingly, NP cells in the kidney organoid experiments were either enriched in the corner or diminished in tip according to
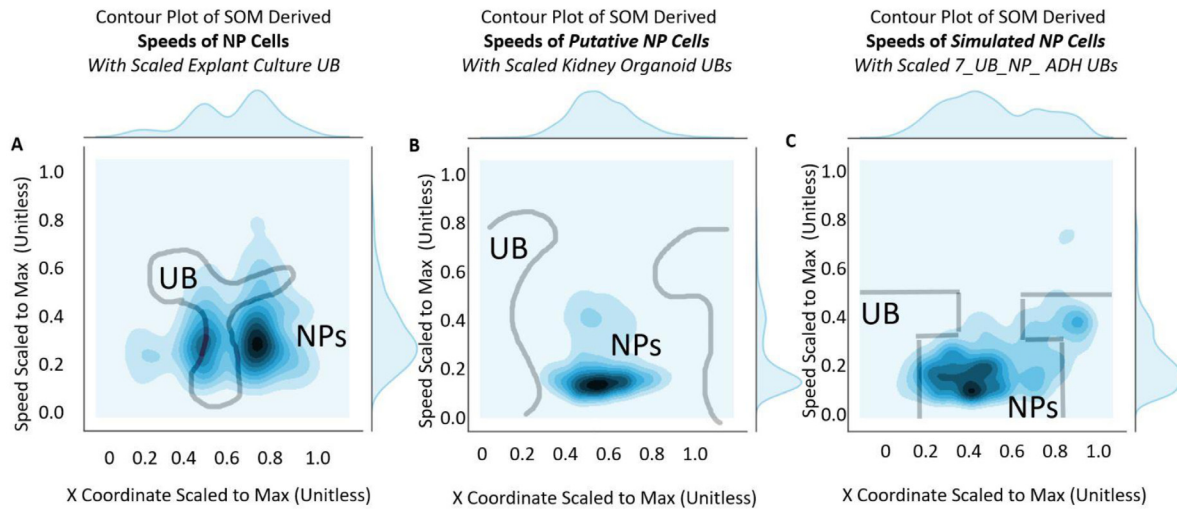
Fig. 7. The cell speed contours of the best SOM groups (see supplement [30]). (A) NP cells in the explant kidney culture [9]. (B) MM cells in the kidney organoid model. (C) NP cells in the optimized model seven. The speeds and the coordinates (x) have been scaled between (0,1). The experimental and simulation images in the background reflect the cell regions.

Table 2
Optimized parameter values for each model variant (1–8). Values are presented as: Random (Uniform), e.g. for NP_ADH: 7.9 (13). {*} 8_ADH_ADH assumed nine cell–cell adhesion interfaces: {1–3} 'UB surface and NP/MM/Medium', {4} 'NP and NP', {5} NP and MM, {6} 'MM and MM', and {7–9} 'Medium and NP/MM/Medium'. The parameters of spatial relationships (V_t, A_t, λ_V, NO), except λ_S, and the ones not mentioned here were constant (see Table 1). The given PSO quality values are the lowest ones that the optimization found.

	REF (1)	ADH (2)	UB (3)	NP (4)	UB_ADH (5)	NP_ADH (6)	UB_NP_ADH (7)	ADH_ADH (8)
Chemoattractant secretion rate (DU/s)	0	0	3	3	3	3	**6.91**	0
Chemotaxis lambda (10^{-27}; kg m^2 s^{-2})	0	0	**4.22 (4.19)**	67.94 (71.3)	43.9 (43.8)	74.5 (74.3)	**1.41**	0
Global diffusion constant (10^{-12}; m^2 s^{-1})	0	0	1	1	1	1	**1.83**	0
Global decay constant (s)	0	0	1×10^{-7}	0.002	1×10^{-7}	0.002	**4.69×10^{-7}**	0
Surface motility (Potts "temperature") (DU)	**10**	25	25	25	25	25	**49.8**	25
Surface lambda (10^{-3}; kgm^{-2} s^{-2})	0.01	0.01	0.01	0.01	0.01	0.01	**8.11**	0.01
Adhesion differences between cell types (10^{-15}; kg s^{-2})	5.0 {5}	**7.9{5}**	5.0 {5}	5.0 {5}	6.68 {5} (6.98 {5})	7.9 {5} (13 {5})	7.86 {5}	21.1 {1}, 25.2 {2},1.75 (3), 0.50 {4},33.3 {5}, 37.7 {6}, 35.8 {7}, 29.7 {8},1.57 {9} (26.6 {1}, 47.8 {2},29.5 (3), 0.50 {4},20.5 {5}, 0.52 {6}, 24.1 {7}, 1.54 {8},38.1 {9})
PSO quality value	−61,269	−56,436	−201,902	−206,525		−205,261	−213,787	−340,361

Table 3
Synopsis of qualitative simulation results before and after optimization (c.f., Figs. 6 and 8).

	REF	ADH	UB	UB_ADH	NP	NP_ADH	UB_NP_ADH	ADH_ADH
Explant culture								
Tip/corner speeds of NP cells	–	–	Divergent	Divergent	–	–	–	–
Quantity of NP cells at corner	–	–	Convergent	Convergent	Divergent	Divergent	Convergent	–
Tip/corner speeds of NP cells (**optimized**)	–	–	Convergent	Convergent	–	–	Convergent	–
Quantity of NP cells at corner (**optimized**)	–	–	Convergent	Convergent	Divergent	Convergent	Convergent	–
Organoid culture								
Tip/corner speeds of MM cells	–	–	–	–	Convergent	Convergent	–	Convergent
Quantity of MM cells at corner	–	–	–	–	Convergent	Convergent	Convergent	–
Tip/corner speeds of MM cells (**opt.**)	–	–	–	–	Convergent	Convergent	Convergent	Convergent
Quantity of MM cells at corner (**opt.**)	–	–	–	–	Convergent	Convergent	–	Convergent

the optimized UB secreting models (c.f., Figs. 8A/B and S4A/B). On the other hand, MM cell quantities in the explant culture experiments increased in the tip similarly as in the optimized NP secreting models or vice versa in the corner (c.f., Figs S4C/D and 8C/D). The cell quantity and speed trends between the model simulations and experiments are compared qualitatively in more detail at Table 3.

4. Discussion

In this work we used a computational modelling approach to explore the biophysical mechanisms driving committed nephron progenitor cells to form proximal tubular aggregates, the early nephron precursor structure during kidney organogenesis. The movements and
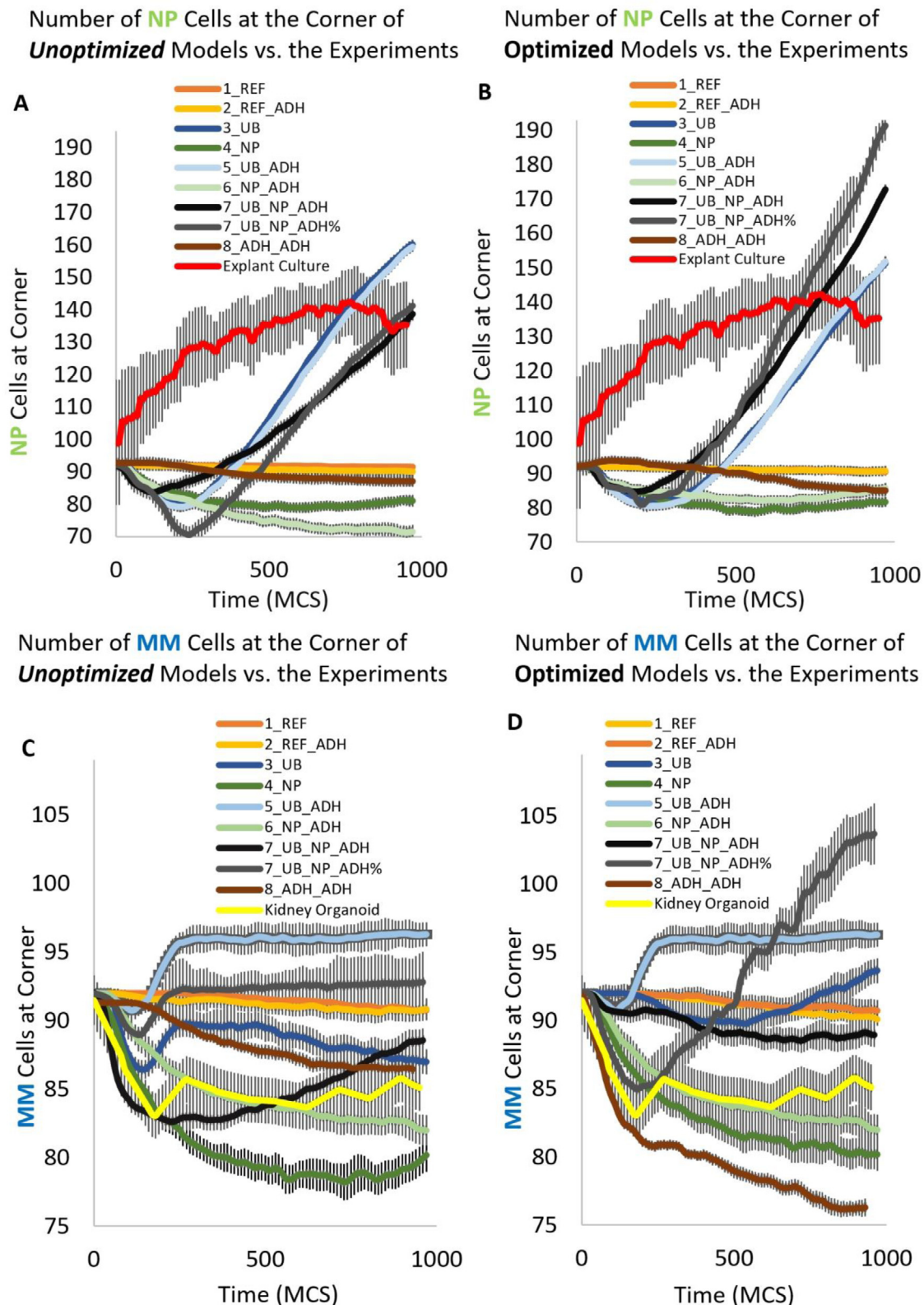
Fig. 8. Enrichment of NP and MM cells in the corner region of the simulation studies of different models together with results from experiments. (A/B) NP cells in the models (see legend) with the cells in the explant culture experiments (scaled to model 3 and 4) [9]. Model 7 is presented with NP cell quantities of 50% (black; regular) and 25% (grey; scaled). (C/D) MM cells in the similar models with cells in the kidney organoid experiments (see legend). (A/C) Simulations before the optimization. (B/D) Simulations after the optimization. Vertical bars indicate 95% confidence intervals from simulations (sample size: 30) or experiments (sample sizes of 50 and 15 for explant and kidney experiments, respectively).

aggregations of the cap mesenchyme cells were studied using a Cellular Potts Model, which was modulated to simulate the relative impact of

chemotaxis and cell–cell adhesion forces. The movement of nephron progenitor cells towards the corner regions of the branching ureteric

bud and the formation of cell aggregates was best reproduced by assuming a combination of chemotactic and differential cell adhesion forces. The parameter estimates were validated and optimized by analysis of cell behaviour in two experimental models of early nephrogenesis. We observed, both *ex vivo* and *in silico*, an increasing speed of committed NP cells as they migrate from the UB tip to the corner region.

Cap mesenchyme cells have been described to move in a quasi-stochastic fashion between the corner and tip regions of the branching ureteric buds (UB) following certain environmental cues [9,22]. While the bulk of metanephric mesenchymal (MM) cells have been considered as static, an emerging subpopulation, the nephron progenitor (NP) cells, is believed to move linearly from the UB tip to the corner region [8]. In order to reproduce these movement patterns *in silico* several assumptions had to be made; these related to the initial spatial structure, cell quantities and properties and were founded on both experimental evidence and on established insights into cellular biophysics.

General assumptions included the assertion that all, and only, NP cells were committed to the formation of PTA, and that changes in three main energies should affect the movements and aggregations of NP and MM cells, i.e. contact surface energies, chemotaxis energy, and cell size changes. The impact of cell sizes was minimal since the initial most expansive phases were discounted in the simulation, leaving chemotaxis and cell–cell adhesion as the main energies to drive cell sorting between regions.

Indeed, there is substantial experimental evidence supporting the notion that the sorting of NP cells between the tip and corner regions is established by cell–cell adhesion differences and both inductive and chemotactic molecular signalling from the ureteric bud epithelia [15, 41,42]. Previous studies identified cell–cell adhesion molecules such as cadherins, to drive cell sorting [15,23]. Extracellular signals inducing NP cell commitment involve the secretion of WNT11, BMP7, FGF9, and WNT9B, which upregulates Wnt4 [3]. NP cell induction has also been shown to involve the activation of Notch and additional signalling pathways [43,44]. At the same time, MM cells require SMAD1/5-mediated BMP signalling to transition towards a state in which they can receive the inductive cues [41]. While WNT9B was the first secreted molecule attributed a role as a chemoattractant for NP cells, subsequent studies identified PDGF-AA, FGF8, BMP4 and CXCL12 as further potential effectors driving NP cell chemotaxis [45–48]. Recently, evidence has been provided that NP cells within the UB tip region do not move in a linear fashion but exhibit a nearly stochastic swarm-like behaviour [9]. Moreover, NP cell commitment and migration towards the corner region may not be a unidirectional, irreversible process: a subset of NP cells at the corner region were observed to migrate back to the tip region to re-enter the uncommitted MM cell pool, losing Wnt4 expression [22]. This behaviour was tentatively explained by semi-stochastic cell movement with exposure of NP cells to different cues depending on their spatial position, with prolonged or additional signals to NP cells being required for persistent clustering in the corner region and PTA formation.

We performed various model simulations to test the impact of chemotaxis and adhesion driven cell sorting on NP cell trafficking and clustering towards the region where PTA could be formed. The initial model setup and simulation studies were followed by a validation and optimization step, where explant culture and organoid experiments were utilized to further align the model parameters to fit the cell movements and aggregations observed *ex vivo*.

Our simulation studies support an important role of chemoattractant gradients arising from the UB surface for net directed NP cell movement. The model variants lacking UB chemoattractant secretion resulted in ectopic NP cell aggregation. Moreover, differential cell–cell adhesion properties appear to be required for the formation of NP cell aggregates. Paracrine chemotactic signalling by NP cells may play a role in this process as suggested by the optimal performance observed with a model combining adhesion differences with chemoattractant secretion by both the UB and the NP cells in the model 7.

Our model also adequately recapitulated the semi-stochastic movement of NP cells around the ureteric buds. Both the average cell speed and their net travelled distance fitted the speeds and distances observed in the explant culture system. Notably, with the model 7 we even observed individual cells returning from the corner to the tip region, in keeping with recent experimental findings [22].

Another notable finding, obtained both in the analysis of the explant culture data and by computational modelling and confirmed by self-organized speed mapping, is the faster NP cell speed in the corner as compared to the tip region. Our model simulations indicated that the acceleration of NP cells approaching the UB corner is due to the chemoattractant concentration present in this region.

The behaviour of cells in the dissociation–reaggregation kidney organoid culture experiments was more challenging to simulate since no marker differentiating native MM from committed NP cells was available. As in the explant culture study, persistently faster cell movement was observed for cells in the corner and slower speed for those in the tip region. In contrast to the explant culture studies where our model simulations pointed to the UB as the predominant source of chemoattractant, regional cell speeds and quantities in the organoid studies were best approximated by the simulation assuming chemoattractant release from NP cells in addition to differences in cell–cell adhesion energies (model 6) [32]. This difference might have been caused by altered secretory functions of the ureteric bud epithelia following cell dissociation and reaggregation, and by the shorter experimental time period utilized in the kidney organoid model which was primarily designed to study early MM cell movement patterns. Nonetheless, the model 6 indicates that mesenchymal cell movement may be primarily driven by auto/paracrine chemotaxis of mesenchymal cells.

While our work demonstrates the suitability of a relatively simple computational model to reproduce the main cellular events in early nephrogenesis, several limitations should be emphasized. First, we did not allow for continuous recruitment of NP cells from the MM cell pool but assumed fixed cell quantities during the time window of analysis. Also, the lack of *in vitro* models deficient in individual components of the biological system prevented an external validation of the performance of our model in simulating impairments of nephrogenesis under abnormal conditions. Finally, the current model system did not allow to explore the roles of individual molecular signalling pathways or more than a single chemoattractant gradient. Such models would have required far more granular biochemical information both of the chemical gradient processes and the PTA niche cell specifications than currently available. Given these limitations, it is even more remarkable that NP cell migration and PTA formation can be accurately modelled based on two biophysical mechanisms, i.e. chemotaxis and cell–cell adhesion differences.

5. Conclusions

In conclusion, we established, validated, and applied a three-dimensional computational model of early nephrogenesis which describes the migration and initial aggregation of nephron progenitor cells as a function of stochastic swarming, chemotaxis and cell-specific adhesion properties. Our simulations suggest chemoattractant secretion by both the ureteric bud epithelia and the nephron progenitor cells themselves. Both experimentally and by simulation a non-linear migration pattern was observed, with cell movement accelerating while moving from the ureteric bud tip to the corner region. Our work demonstrates that computational modelling can aid in interpreting experimental data to reveal underlying biophysical mechanisms. The proposed model may be used as a starting point for more refined model systems as new molecular insights and experimental settings with higher information content become available.

Availability of data and materials

The data of explant culture experiments have been published [9]. The data of this work, including the experimental data in the kidney organoid and the analysis codes, have been uploaded to public repositories [32,39,40]. The segmentation codes for the kidney organoid model are available at [14].

Embryonic kidneys were dissected from embryonic day 11.5 mouse embryos from crossing of Wnt4Cre [33] was generated in the laboratory of Professor Seppo Vainio, University of Oulu, Finland, and tomato floxed Rosa26 Green fluorescent protein (GFP; mT/mG) reporter mice [34] was purchased by University of Oulu from The Jackson Laboratory (Stock No. 007676).

CRediT authorship contribution statement

Pauli Tikka: Primary conceptual and programming work, Drafted the manuscript. **Moritz Mercker:** Writing the manuscript, Model and analysis related questions. **Ilya Skovorodkin:** Conducted the kidney organoid experiments. **Ulla Saarela:** Conducted the kidney organoid experiments. **Seppo Vainio:** Revisioning of the text. **Veli-Pekka Ronkainen:** Calibration of the microscopes and segmentation method. **James P. Sluka:** Developing the model in CompuCell3D, PSO simulations. **James A. Glazier:** Developing the model in CompuCell3D, PSO simulations. **Anna Marciniak-Czochra:** Revisioning of the text. **Franz Schaefer:** Writing the manuscript.

Declaration of competing interest

The authors declare that they have no known competing financial interests or personal relationships that could have appeared to influence the work reported in this paper.

Data availability

My code is available at GitHub: https://github.com/paulitikka. The data can be found at: https://figshare.com/authors/paulitt1_hotmail_com_paulitt1_hotmail_com/7873955.

Ethics approval and consent to participate

Animal care and procedures were in accordance with Finnish national legislation for the use of laboratory animals, the European Convention for the protection of vertebrate animals used for experimental and other scientific purposes (ETS 123), and the EU Directive 86/609/EEC. The mouse studies were approved by an ethics committee as mentioned in the methods.

Appendix A. Supplementary data

Supplementary material related to this article can be found online at https://doi.org/10.1016/j.mbs.2021.108759.

References

[1] M. Krause, A. Rak-Raszewska, I. Pietila, S.E. Quaggin, S. Vainio, Signaling during kidney development, Cells 4 (2015) 112–132, http://dx.doi.org/10.3390/cells4020112.

[2] J. Blake, N.D. Rosenblum, Renal branching morphogenesis: morphogenetic and signaling mechanisms, Semin. Cell Dev. Biol. 36 (2014) 2–12, http://dx.doi.org/10.1016/j.semcdb.2014.07.011.

[3] T. Bohnenpoll, A. Kispert, Ureter growth and differentiation, Semin. Cell Dev. Biol. 36 (2014) 21–30, http://dx.doi.org/10.1016/j.semcdb.2014.07.014.

[4] F. Costantini, R. Kopan, Patterning a complex organ: branching morphogenesis and nephron segmentation in kidney development, Dev. Cell 18 (2010) 698–712, http://dx.doi.org/10.1016/j.devcel.2010.04.008.

[5] A. Desgrange, S. Cereghini, Nephron patterning: lessons from xenopus, zebrafish, and mouse studies, Cells 4 (2015) 483–499, http://dx.doi.org/10.3390/cells4030483.

[6] T.K.J. Obara-Ishihara, L. Niswander, D. Herzlinger, The surface ectoderm is essential for nephric duct formation in intermediate mesoderm, Development 126 (1999) 1103–1108.

[7] P.L. Whetzel, et al., BioPortal: enhanced functionality via new Web services from the National Center for Biomedical Ontology to access and use ontologies in software applications, Nucl. Acids Res. 39 (2011).

[8] M.H. Little, A.P. McMahon, Mammalian kidney development: principles, progress, and projections, Cold Spring Harb. Perspect. Biol. 4 (2012) http://dx.doi.org/10.1101/cshperspect.a008300.

[9] A.N. Combes, J.G. Lefevre, S. Wilson, N.A. Hamilton, M.H. Little, Cap mesenchyme cell swarming during kidney development is influenced by attraction, repulsion, and adhesion to the ureteric tip, Dev. Biol. 418 (2016) 297–306, http://dx.doi.org/10.1016/j.ydbio.2016.06.028.

[10] A.P. McMahon, Development of the mammalian kidney, Curr. Top. Dev. Biol. 117 (2016) 31–64, http://dx.doi.org/10.1016/bs.ctdb.2015.10.010.

[11] S. Chen, et al., Intrinsic age-dependent changes and cell–cell contacts regulate nephron progenitor lifespan, Dev. Cell 35 (2015) 49–62, http://dx.doi.org/10.1016/j.devcel.2015.09.009.

[12] P. Chi, Y. Kwon, D.N. Moses, C. Seong, M.G. Sehorn, et al., Functional interactions of meiotic recombination factors Rdh54 and Dmc1, DNA Repair. (Amst.) 8 (2009) 279–284.

[13] M.H. Little, Kidney Development, Disease, Repair and Regeneration, first ed., Academic Press, 2015.

[14] U. Saarela, et al., Novel fixed z-direction (FiZD) kidney primordia and an organoid culture system for time-lapse confocal imaging, Development 144 (2017) 1113–1117, http://dx.doi.org/10.1242/dev.142950.

[15] J.G. Lefevre, et al., Self-organisation after embryonic kidney dissociation is driven via selective adhesion of ureteric epithelial cells, Development 144 (2017) 1087–1096, http://dx.doi.org/10.1242/dev.140228.

[16] A.T. Dudley, R.E. Godin, E.J. Robertson, Interaction between FGF and BMP signaling pathways regulates development of metanephric mesenchyme, Genes Dev. 13 (1999) 1601–1613, http://dx.doi.org/10.1101/gad.13.12.1601.

[17] E. Wallner, Q. Yang, D. Peterson, J. Wada, Y. Kanwar, Relevance of extracellular matrix, its receptors, and cell adhesion molecules in mammalian nephrogenesis, Am. J. Physiol. 275 (1998) F467–477, http://dx.doi.org/10.1152/ajprenal.1998.275.4.F467.

[18] U. Dahl, et al., Genetic dissection of cadherin function during nephrogenesis, Mol. Cell Biol. 22 (2002) 1474–1487, http://dx.doi.org/10.1128/mcb.22.5.1474-1487.2002.

[19] L. Oxburgh, A.C. Brown, J. Fetting, B. Hill, BMP signaling in the nephron progenitor niche, Pediatr. Nephrol. 26 (2011) 1491–1497, http://dx.doi.org/10.1007/s00467-011-1819-8.

[20] R. Magno, V.A. Grieneisen, A.F. Maree, The biophysical nature of cells: potential cell behaviours revealed by analytical and computational studies of cell surface mechanics, BMC Biophys. 8 (2015) 8, http://dx.doi.org/10.1186/s13628-015-0022-x.

[21] M.H. Swat, et al., Multi-scale modeling of tissues using compucell3d, Methods Cell Biol. 110 (2012) 325–366, http://dx.doi.org/10.1016/B978-0-12-388403-9.00013-8.

[22] K.T. Lawlor, et al., Nephron progenitor commitment is a stochastic process influenced by cell migration, eLife 8 (2019) e41156, http://dx.doi.org/10.7554/eLife.41156.

[23] S. Junttila, et al., Functional genetic targeting of embryonic kidney progenitor cells ex vivo, J. Am. Soc. Nephrol. 26 (2015) 1126–1137, http://dx.doi.org/10.1681/ASN.2013060584.

[24] A.N. Combes, et al., An integrated pipeline for the multidimensional analysis of branching morphogenesis, Nat. Protoc. 9 (2014) 2859–2879, http://dx.doi.org/10.1038/nprot.2014.193.

[25] N.O. Lindström, et al., Progressive recruitment of mesenchymal progenitors reveals a time-dependent process of cell fate acquisition in mouse and human nephrogenesis, Dev. Cell 45 (2018) 651–660, http://dx.doi.org/10.1016/j.devcel.2018.05.010, e654.

[26] M.H. Swat, et al., Multicell simulations of development and disease using the compucell3d simulation environment, Methods Mol. Biol. 500 (2009) 361–428, http://dx.doi.org/10.1007/978-1-59745-525-1_13.

[27] V. Andasari, R.T. Roper, M.H. Swat, M.A. Chaplain, Integrating intracellular dynamics using compucell3d and bionetsolver: applications to multiscale modelling of cancer cell growth and invasion, PLoS One 7 (2012) e33726, http://dx.doi.org/10.1371/journal.pone.0033726.

[28] T. Hirashima, E.G. Rens, R.M.H. Merks, Cellular potts modeling of complex multicellular behaviors in tissue morphogenesis, Dev. Growth Differ. 59 (2017) 329–339, http://dx.doi.org/10.1111/dgd.12358.

[29] J.M. Osborne, A.G. Fletcher, J.M. Pitt-Francis, P.K. Maini, D.J. Gavaghan, Comparing individual-based approaches to modelling the self-organization of multicellular tissues, PLoS Comput. Biol. 13 (2017) e1005387, http://dx.doi.org/10.1371/journal.pcbi.1005387.

[30] T. Kohonen, Self–organized formation of topologically correct feature maps, Biol. Cybernet. 43 (1982) 59–68, http://dx.doi.org/10.1007/BF00337288.

[31] G. Vettigli, Minisom self organizing maps, 2018, <https://github.com/JustGlowing/minisom>.

[32] P. Tikka, Data of non-optimized and optimized CC3D models and kidney organoid experiments, 2019, <https://figshare.com/projects/Research_Data/71801>.

[33] J. Shan, T. Jokela, I. Skovorodkin, S. Vainio, Mapping of the fate of cell lineages generated from cells that express the Wnt4 gene by time-lapse during kidney development, Differentiation 79 (2010) 57–64, http://dx.doi.org/10.1016/j.diff.2009.08.006.

[34] M.D. Muzumdar, B. Tasic, K. Miyamichi, L. Li, L. Luo, A global double-fluorescent Cre reporter mouse, Genesis 45 (2007) 593–605, http://dx.doi.org/10.1002/dvg.20335.

[35] P. Tikka, I. Skovorodkin, The video of kidney organoid experiments, 2019.

[36] A.C. Brown, D. Adams, M. de Caestecker, X. Yang, R. Friesel, FGF/EGF signaling regulates the renewal of early nephron progenitors during embryonic development, Development 138 (2011) 5099–5112, http://dx.doi.org/10.1242/dev.065995.

[37] P. Müller, et al., Differential diffusivity of nodal and lefty underlies a reaction-diffusion patterning system, Science 336 (2012) 721, http://dx.doi.org/10.1126/science.1221920.

[38] P. Tikka, Tikka P Video of model 7, 2019, <https://figshare.com/articles/Optimized_Model_7_s_video/10315904>.

[39] P. Tikka, Tikka P Model data analysis, 2019, <https://github.com/paulitikka/Model-Data-Analysis>.

[40] P. Tikka, CC3D model example codes, 2019, <https://github.com/paulitikka/CC3D-Model-Example-Codes>.

[41] A.C. Brown, et al., Role for compartmentalization in nephron progenitor differentiation, Proc. Natl. Acad. Sci. USA 110 (2013) 4640–4645, http://dx.doi.org/10.1073/pnas.1213971110.

[42] C.M. Karner, et al., Canonical Wnt9b signaling balances progenitor cell expansion and differentiation during kidney development, Development 138 (2011) 1247–1257, http://dx.doi.org/10.1242/dev.057646.

[43] N.O. Lindstrom, et al., Integrated beta-catenin, BMP, PTEN, and Notch signalling patterns the nephron, elife 3 (2015) e04000, http://dx.doi.org/10.7554/eLife.04000.

[44] A.O. Perantoni, et al., Inactivation of FGF8 in early mesoderm reveals an essential role in kidney development, Development 132 (2005) http://dx.doi.org/10.1242/dev.01945.

[45] U. Grieshammer, et al., FGF8 is required for cell survival at distinct stages of nephrogenesis and for regulation of gene expression in nascent nephrons, Development 132 (2005) 3847–3857, http://dx.doi.org/10.1242/dev.01944.

[46] Y. Atsuta, Y. Takahashi, FGF8 coordinates tissue elongation and cell epithelialization during early kidney tubulogenesis, Development (Camb. Engl.) 142 (2015) 2329–2337, http://dx.doi.org/10.1242/dev.122408.

[47] J.M. Ricono, B. Wagner, Y. Gorin, M. Arar, A. Kazlauskas, PDGF receptors modulates metanephric mesenchyme chemotaxis induced by PDGF-AA, Am. J. Physiol. Ren. Physiol. 296 (2008) F406–F417, http://dx.doi.org/10.1152/ajprenal.90368.2008.

[48] T.J. Carroll, J.S. Park, S. Hayashi, A. Majumdar, A.P. McMahon, Wnt9b plays a central role in the regulation of mesenchymal to epithelial transitions underlying organogenesis of the mammalian urogenital system, Dev. Cell 9 (2005) 283–292, http://dx.doi.org/10.1016/j.devcel.2005.05.016.